Visualizing the molecular recognition trajectory

of an intrinsically disordered protein using

multinuclear relaxation dispersion NMR

Authors:

Robert Schneider[1,†], Damien Maurin[1], Guillaume Communie[1], Jaka Kragelj[1], D. Flemming Hansen[2], Rob W.H. Ruigrok[3], Malene Ringkjøbing Jensen[1], Martin Blackledge[1,*]

Affiliations:

[1a]Univ. Grenoble Alpes, IBS, 38044 Grenoble, France. [1b]CNRS, IBS, 38044 Grenoble, France. [1c]CEA, IBS, 38044 Grenoble, France. [2]Institute of Structural and Molecular Biology, Division of Biosciences, University College London, Gower street, London WC1E 6BT, United Kingdom, [3a]Univ. Grenoble Alpes, UVHCI, 38000 Grenoble, France, [3b]CNRS, UVHCI, 38000 Grenoble, France, [3c]Unit for Virus Host-Cell Interactions, Univ. Grenoble Alpes-EMBL-CNRS, 38000 Grenoble France. [†]Present address: Université Lille 1, UMR CNRS 8576, Cité Scientifique, Bât. C9, 59655 Villeneuve d'Ascq Cedex, France.

KEYWORDS Nuclear Magnetic Resonance, Intrinsically disordered protein, Relaxation dispersion, folding upon binding, protein dynamics, conformational funnelling

Communicating author:

martin.blackledge@ibs.fr

Abstract: Despite playing important roles throughout biology, molecular recognition mechanisms in intrinsically disordered proteins remain poorly understood. We present a combination of $^1H^N$, $^{13}C'$ and ^{15}N relaxation dispersion (RD) NMR, measured at multiple titration points, to map the interaction between the disordered domain of Sendai virus nucleoprotein (NT) and the C-terminal domain of the phosphoprotein (PX). Interaction with PX funnels the free-state equilibrium of NT by stabilizing one of the previously identified helical sub-states present in the pre-recognition ensemble, in a non-specific and dynamic encounter complex on the surface of PX. This helix then locates into the binding site at a rate coincident with intrinsic breathing motions of the helical groove on the surface of PX. The binding kinetics of complex formation are thus regulated by intrinsic free-state conformational dynamics of both proteins. This approach, providing high-resolution structural and kinetic information about a complex folding and binding interaction trajectory, can be applied to a number of experimental systems to provide a general framework for understanding conformational disorder in biomolecular function.

INTRODUCTION

Intrinsically disordered proteins (IDPs) are abundant throughout biology,[1–4] in particular in eukaryotic proteomes and in some viruses,[5] playing crucial roles for example in signaling pathways or regulation of transcription and replication.[6] Biological function of IDPs is often mediated by short sequences of peptides, known as linear motifs, that control a vast range of cellular processes through interactions with structured partner proteins.[7,8] In spite of the ubiquitous nature of IDPs, the exact molecular mechanisms regulating their interactions with physiological partners remains poorly understood. This is of prime importance because many IDPs are involved in human disease.[9] The development of rational pharmacological strategies awaits a detailed understanding of the molecular basis of biological interaction and function in this extensive but poorly understood fraction of the human proteome. IDPs exhibit highly heterogeneous local and long-range structural and dynamic propensities, and this sequence-dependent conformational behavior is thought to play a key role in regulating function. Considerable effort has therefore been devoted to the development of robust approaches to describe conformational heterogeneity in IDPs,[10–15] and its relationship to functional properties such as recognition of physiological partners.[16–19]

The relationship between free- and bound-state conformational behaviour is however not straightforward,[20] as exemplified by the observation of promiscuous IDPs adopting distinct conformations of the same binding sites in complex with different interaction partners.[21] Depending on the relative importance of enthalpic and entropic contributions, either pre-folded or unfolded forms may be considered more likely to mediate binding via conformational selection or induced-fit type interactions.[22–25] The mechanisms underpinning the kinetics of IDP interactions are rendered yet more complex by the suggestion that some complexes involving IDPs remain dynamic even in interaction with their partners.[26] Although a growing body of theoretical,[27–30] numerical[31–34] and kinetic studies [35–37] have been used to

predict or globally characterize molecular recognition in IDPs, these processes remain largely unexplored at atomic resolution.[38]

NMR studies of interactions involving IDPs are often hampered by excessive line broadening, because exchange between free and bound conformations often occurs on time-scales that give rise to intermediate exchange broadening (in the millisecond range), precluding direct detection of the bound-state peaks. It is possible to investigate the origin of this line broadening, by detecting the free-state, at low titration admixtures of the partner protein, where the resonance-peak is only weakly broadened. Under these conditions, where the bound-state represents a weakly populated minor state, relaxation dispersion (RD) NMR[39,40] can be used to investigate the structure, population and inter-conversion rates of the otherwise invisible bound-state equilibrium.[16]

In this study we use RD, measured for multiple nuclei (^{15}N, ^{13}C' and ^{1}H^{N}) and at multiple admixtures of the intrinsically disordered C-terminal domain of Sendai virus nucleoprotein (NT, residues 401-524) and the partially folded C-terminal head-group of the phosphoprotein (PX, residues 474-568), to develop a detailed description of the trajectory from the free state equilibrium to the bound-state. Changes in ^{13}C chemical shifts predominantly report on changes in secondary structure formation,[41] while changes in ^{15}N and ^{1}H shifts are particularly sensitive to the tertiary interactions formed at the binding interface of two proteins. The combination of these complementary sources of information proves to be crucial for describing the intricate interaction pathway.

Sendai virus belongs to the paramyxoviridae genus, within which the important human pathogens Measles, Nipah and Hendra share homologous PX and NT domains.[42,43] The NT:PX interaction in this viral family is thought to play an essential role in replication *in vivo*, by initiating the interaction between the viral polymerase and genome.[44] The NT:PX

interaction is central to the viral replication machinery, and as such represents an important and viable target for rational drug design in this class of viruses.

We have previously used NMR residual dipolar couplings to characterize the conformational equilibrium of unbound NT, revealing an interaction site sampling three distinct, differently populated N-capped[45] helical sub-states, in rapid exchange with a completely unfolded population.[46,47] This linear motif is thought to further fold upon binding to PX,[48] on the basis of the crystal structure of a chimeric construct of the homologous NT:PX complex from Measles virus.[49,50] NT is an ideal system with which to investigate folding and binding interactions, because of the detailed understanding of the intrinsic conformational sampling of the free form of the protein. Our aim is to map the entire interaction trajectory, and in particular to determine whether the nature of the free-state ensemble, in particular the different pre-folded conformations present comprising the equilibrium, play any role in the molecular recognition process.

RESULTS

NMR relaxation dispersion studies of the NT:PX interaction

NMR chemical shift titration studies of the NT:PX complex show that resonances of NT from throughout the interaction region (residues 473 to 492) experience line broadening (Fig. S1). In this exchange regime NMR titration only provides an estimate of the dissociation constant $K_d < 60$ μM.[48] Here we also present isothermal titration calorimetry (ITC) measurements, which allow a more precise determination of $K_d = 8.4 \pm 0.9$ μM (Fig. S2). In order to identify the molecular mechanisms giving rise to the observed broadening of these resonances, ^{15}N, $^{13}C'$ and $^1H^N$ RD experiments were performed on NT (401-524) at two magnetic fields (14.1 and 18.8 T) and at admixtures ranging from 0 to 0.15 molar ratios of PX (see Methods). No detectable RD is measured in free NT (Fig. S3), confirming the rapid nature of the exchange between the three helical sub-states and the unfolded state. However,

even at the smallest PX:NT molar ratio (0.02), RD is measured throughout the previously identified[46,48] molecular recognition element for all three types of nuclei (Fig. 1 and S4). No exchange is detectable using RD from regions outside the helical element, for any admixture. We note that most resonances from the molecular recognition element are broadened beyond detection at PX:NT molar ratios higher than (0.20) (Fig. S5).

More than 700 experimental RD curves were measured from throughout the molecular recognition element. Examination of the measured dispersion curves reveals a complex distribution, with clear differences in exchange contributions to $R_{2,eff}$ from the different nuclei for distinct peptide units. For example, while backbone carbonyl groups experience continuous exchange contributions between residues 474-479, and 486-492, the central section of the helical region, comprising residues 480-484, exhibits weaker $^{13}C'$ dispersion and larger ^{15}N exchange contributions (Fig. 1).

Analysis of RD data from the molecular recognition site in terms of a two-state binding model

Data were analyzed using the following approaches: Firstly, for each admixture all data from each individual peptide plane (^{15}N and $^{1}H^{N}$ of residue *i* and $^{13}C'$ of residue *i*-1) in the helical region were simultaneously analyzed using a two-site exchange model,[51,52] to determine the chemical shift differences ($\Delta\omega$) between the free form and the bound state, the residue-specific exchange rates (k_{ex}) and the bound state populations (p_B) (Fig S6). The analysis was repeated, simultaneously analyzing all data for each individual peptide plane from 2-8% admixtures of PX, assuming residue-specific exchange rates (Fig. S7). In both cases a non-uniform k_{ex} is observed along the primary sequence, with rates in the 474-478 and 486-489 range clustering between 700 and 800s^{-1}, and residues in the central region exhibiting higher or lower rates (Fig. 2A). This variability of k_{ex} is associated with a non-uniform distribution of p_B values (Fig. 2B). Importantly, simultaneous analysis of all data at individual titration

mixtures using common k_{ex} and p_B values also demonstrates that while the majority of curves are reproduced by k_{ex} of $771\pm38s^{-1}$ (Fig. S8) a number of curves, in particular those showing large ^{15}N dispersion, are very poorly reproduced (representative examples shown in Fig. 3).

Analysis of RD data from the molecular recognition site in terms of a three-state binding model

The observation of heterogeneous exchange rates and populations over the helical region, and the inability of a global 2-state exchange approach to acceptably reproduce all experimental data, suggests that this model is insufficient to explain the NT:PX interaction. We have therefore tested linear 3-state exchange models (see Methods). Although the parametric space available from such a 3-state fit is ill-defined, inherent degeneracy is raised by the combination of the ^{13}C', ^{15}N and $^1H^N$ RD data. As an example, the most complete data set, measured at 0.05 PX:NT ratio, provide a convergent fit to a linear exchange model, yielding a global minimum centered around $k_{AB}=(852\pm31)s^{-1}$ and $k_{BC}=(2600\pm493)s^{-1}$, with $p_B=3.7\pm0.1\%$ and $p_C=1.3\pm0.1\%$ (Fig. 4 and Fig. S9). RD data measured at the other individual admixtures are closely consistent with this model (Fig. 4). Improvement in data reproduction (Fig 3, Table 1) using the more complex model measured over the entire data set is statistically significant for all individual molar ratios ($p<0.0001$ at [PX]/[NT]=0.05, 0.08, and 0.15; $p<0.01$ at [PX]/[NT]=0.35, Table 1) with the exception of [PX]/[NT]=0.02, probably due to the low amplitude of the RD phenomena at this admixture. Equally importantly, fitted p_B and p_C values for admixtures other then 5% fall closely within the range expected from the K_d of the interaction (Fig. 5 and S10). A combined analysis, fitting all admixtures simultaneously using a 3-state model, resulted in similar $\Delta\omega_{AB}$ and $\Delta\omega_{AC}$ values as the individual admixtures (Fig. S11) and resulted in similar kinetic and theremodynamic parameters ($k_{AB}=(884\pm99)s^{-1}$ and $k_{BC}=(2374\pm590)s^{-1}$, $p_B=3.3\pm0.1\%$ and $p_C=0.9\pm0.1\%$ for 0.05 admixture, see supporting information for remaining admixture populations).

Chemical shifts associated with the different steps along the interaction trajectory

While the first step of the 3-state analysis reproduces features of the best-fit 2-state model ($\Delta\omega_{AB}$, Fig. S12), ^{13}C' shifts associated with the second step ($\Delta\omega_{AC}$ measured relative to the free shifts) are ill-defined for all sites, with the exception for the N and C termini of the helix (Fig. S11 and S13). For residues with pronounced ^{13}C' dispersion in the [PX]/[NT]=0.05 dataset, $\Delta\omega_{AC}$ values reproduce the $\Delta\omega_{AB}$ pattern (Fig. S14), indicating that change in ^{13}C' chemical shift in the second step ($\Delta\omega_{BC}$) is close to zero. ^{13}C' shifts are highly sensitive to secondary structural propensity,[53] so that the first step is likely associated with a shift in helical population. The signs of the ^{13}C' shift changes were determined using previously established approaches,[54] revealing that helices are formed (positive $\Delta\omega$) in the A-B step, rather than removed (negative $\Delta\omega$), upon interaction (Table S1).

The second step (B-C), occurring at the faster rate, affects mainly ^{15}N and ^{1}H^{N} RD measurements (Fig. 6), with generally significantly larger $\Delta\omega$ than in the A-B step. In contrast to the ^{13}C shifts, shifts associated with the second step more closely resemble the 2-state distribution (Fig. S15). Interestingly the ^{1}H^{N} $\Delta\omega$ values appear to map the primary interaction site of NT with PX, with a pronounced helical periodicity observed along the sequence (Fig. 6). Notably, the rate of this step closely corresponds to that of a known exchange process intrinsic to PX (k_{ex}=(2860±160)s^{-1}) interpreted as a breathing motion of PX helices II and III.[55] We note that the presence of two distinct steps in the interaction process may also explain why resonances of NT remain exchange broadened even in the presence of excess PX (Fig. S5).

Analysis of conformational changes associated with the NT:PX interaction

The fitted ^{13}C' $\Delta\omega$ values of NT derived from the three-state analysis were added to the free-state equilibrium isotropic ^{13}C' shifts to determine the chemical shifts in the B and C states. These values were then analyzed in terms of conformation using the minimum ensemble

ASTEROIDS approach (see Methods), starting from a single conformational state, and iteratively testing for the presence of more complex equilibria if simpler models did not adequately reproduce the data.[46,47] Comparison of the experimental shifts with values predicted from all possible helical ensembles spanning the entire molecular recognition element revealed that a single helix (476-489), strongly resembling the H2 helical state (476-488), is stabilized from the free-state equilibrium (Fig. 7). No significant improvement in the data reproduction is achieved when invoking the presence of additional helices in exchange with this helix (Fig. S16). The first step of the interaction therefore appears to report on a population shift from the free-state equilibrium to this single helical state upon interaction with PX.

Characterization of the NT:PX interaction from the perspective of PX

^{15}N and ^{1}H^N RD was also measured on the partner protein PX upon addition of NT (Fig. S17). In agreement with previous results,[55] we observe fast conformational exchange in several residues within helix III of free PX at a rate of $k_{ex}=(2860\pm160)$s^{-1}. Titration of NT induces additional exchange rates corresponding to those measured on NT for the first step of the interaction (803 ± 37)s^{-1} (Fig. 2C and S18), with the residues involved mapping the interaction site of NT along the inter-helical cleft of PX (Fig. 7).

Estimation of association and dissociation rates, electrostatics and mutation studies

Estimates based on the experimentally determined K_d and k_{ex} indicate an association rate, k_{on} in the range of $1.4-4.0\cdot10^7$ M^{-1}s^{-1} (see Methods) significantly exceeding the diffusion limit,[24] and indicating that electrostatic interactions play a role in initial complex formation. We have tested this hypothesis by mutating the negatively charged residues D475 and D478 in the N-terminal part of the NT interaction region to alanines. The results show a slowing of the effective association rate to $4.4\cdot10^6$ M^{-1}s^{-1}, supporting the suggestion that the initial encounter complex is electrostatically driven.

DISCUSSION

The high level of detail with which folding and binding events can be mapped using this combination of $^{13}C'$, ^{15}N and $^{1}H^{N}$ RD, reveals a probable trajectory for formation of the NT:PX complex (Fig. 8). According to this scenario, the interaction pathway follows a two step process, initially funneling the existing conformational equilibrium[56] via stabilization of one of the interconverting helices known to be present in the free-state.[46] This step accounts for the majority of RD-observed $^{13}C'$ chemical shifts, with minimal associated ^{15}N and $^{1}H^{N}$ shifts, suggesting that the initial interaction is non-specific with respect to the surface of PX. Although the local conformation of NT (corresponding to helix H2) is well defined during the intermediate step, we have no information about the relative positioning of NT on the surface of PX, although the lack of significant ^{15}N and ^{1}H shifts associated with this step indicate that it is highly likely that it is dynamic. The second, faster step induces significant ^{15}N and $^{1}H^{N}$ shifts, with the latter reporting on specific binding of one side of the helix in the inter-helical groove on the surface of PX. Remarkably, the rate associated with this second step corresponds closely to the intrinsic conformational exchange rate observed in the helical groove, providing strong evidence that the initial encounter complex is stabilized at a rate dictated by the intrinsic host protein dynamics.

This study thus provides experimental evidence of an IDP interaction mechanism comprising two distinct steps. The rapidly exchanging free-state equilibrium sampled by NT is repopulated upon initial encounter with PX, such that only one helix is present on the surface of PX. Note that we cannot distinguish from the experimental data alone whether stabilization of H2 occurs uniquely through binding of this helical state in a conformational selection-type mechanism, or whether the individual states can each form H2 after encountering PX.[22,24] In either case the overall scenario is retained, consisting of funneling the initial conformational equilibrium into a state resembling H2 in the encounter complex. The final bound state is however not achieved via this initial encounter interaction, which

10

remains non-specific until the second binding event specifically locates NT into the helical groove on the surface of PX.

The possible thermodynamic advantages of formation of a non-specific encounter complex facilitating subsequent localization in the specific partner binding site have been discussed extensively.[22,24,28] In the case of the NT:PX interaction, stabilization of the pre-formed helix presents the advantage that native contacts can be rapidly formed when the final interaction site is located on the surface of PX, a mechanism that is evidently energetically more favorable than complete folding upon binding from the disordered state. The first step, involving stabilization of an existing helical conformation, apparently incurs low enthalpic cost, and is rather associated with a loss of entropy due to depopulation of the more disordered elements of the free state equilibrium. The second step is then driven by the enthalpic benefit associated with formation of specific interactions within the PX binding site.

Interestingly, NMR and stopped-flow studies of the intrinsically disordered ACTR protein, that folds upon binding to its partner NCBD, were used to demonstrate an acceleration of ligand binding as a function of intrinsic helical content,[57] in agreement with our observation that the helical population present in the free-state equilibrium of NT is important for binding. The atomic resolution conformational and thermodynamic analysis presented here provides a mechanistic framework for these observations. By contrast time-resolved stopped-flow measurements, combined with circular dichroism and site-directed mutagenesis, recently indicated that residual structure is not required for binding of the disordered protein PUMA to its partner,[58] indicating rather the presence of a single step, induced-fit type of mechanism. Our analysis of NT:PX reveals a clear two-step process, the first of which shows clear stabilization of one of the existing sub-states present in the free-state equilibrium of NT.

It is also important to note that analysis of only a subset of our experimental data, for example ^{13}C RD curves alone or individual titration measurements, can also be globally explained in terms of a single step mechanism, but that simple two-state models derived from ^{13}C', ^{15}N or ^{1}H^{N} clearly contradict each other, as well as the more complete data set. Only the combination of ^{13}C', ^{15}N and ^{1}H^{N} measurements identifies distinct steps, reporting predominantly either on folding (^{13}C') or binding (^{15}N and ^{1}H^{N}) events in the NT:PX interaction pathway. The intricate trajectory revealed by RD further underlines the complexity of possible binding mechanisms populating the IDP-interactome, and reiterates the necessity for detailed atomic resolution studies to provide mechanistic explanations for these different scenarios.

In conclusion, multinuclear RD provides an atomic resolution map of the molecular recognition trajectory of intrinsically disordered NT from the highly dynamic free-state equilibrium to the PX-bound state, revealing a three state interaction process whose binding modes and kinetics are regulated by the intrinsic conformational equilibrium of NT and the dynamic behavior of PX. This approach, providing high-resolution structural and kinetic information about a complex folding and binding interaction trajectory, can be applied to a number of experimental systems to provide a general framework for understanding conformational disorder in biomolecular function, that will eventually inform rational drug intervention involving this enigmatic class of proteins.

METHODS

Sample preparation

The NT domain comprising residues 401–524 of the nucleoprotein of Sendai virus (SeV) strain Harris, whose amino acid sequence corresponds to that of SeV Fushimi strain NT (UniProtKB accession number Q07097) except for the mutation E410K, as well as the PX domain comprising residues 474–568 of the phosphoprotein (UniProtKB P04859) of SeV

strain Harris, were expressed and purified as described previously.[48] For preparation of NMR samples of $^{13}C,^{15}N$ isotope-labeled NT complexed with unlabeled PX, stock solutions of 208 µM $^{13}C,^{15}N$-NT and 1.15 mM PX were used, both in 50 mM sodium phosphate buffer at pH 6.0 with 500 mM NaCl. The NT stock also contained 9.5% D_2O (vol/vol). From these stocks, admixtures of NT with 2, 3.5, 5, 8 and 15% PX (mol/mol) were made. Final NT:PX concentrations in these admixtures (in µM) were 204:4.1, 176:6.2, 199:9.9, 194:15.5 and 183:27.5, respectively. NMR experiments on free NT were recorded on a sample at a concentration of 305 µM. For samples of ^{15}N isotope-labeled PX alone or complexed with unlabeled NT, a stock solution of 408 µM ^{15}N-PX in 50 mM sodium phosphate, 500 mM NaCl, 1 mM DTT and with 9.5% D_2O (vol/vol) at pH 6.0 was used. Appropriate amounts of a 286 µM stock solution of unlabeled NT (in 50 mM sodium phosphate, 500 mM NaCl, pH 6.0) were added to yield ^{15}N-PX samples with 5, 8, and 15% NT (mol/mol), respectively (final PX: NT concentrations in µM: 378:18.8, 363:29, 331:49.6).

NMR spectroscopy

NMR experiments were performed at sample temperatures of 25°C on Varian/Agilent VNMRS 600 and 800 MHz spectrometers using room-temperature as well as cryogenically cooled triple-resonance HCN probes. All RD experiments employed constant-relaxation-time Carr-Purcell-Meiboom-Gill (CPMG) pulse schemes in which a series of 2D ^{15}N-^{1}H correlation spectra with different CPMG frequencies $\nu_{CPMG} = 1/(2\tau_{CP})$ were recorded, where τ_{CP} is the spacing between successive 180° refocusing pulses. Amide ^{15}N and $^{1}H^{N}$ as well as carbonyl ^{13}C' RD profiles were recorded using pulse sequences described in the literature.[59–61] In the ^{15}N dispersion experiment, ^{1}H continuous-wave decoupling was applied during the CPMG period. Typically, 10–14 points (including 1 or 2 duplicates for error analysis) were recorded for each dispersion curve, corresponding to ν_{CPMG} frequencies between 31.25 and 1000 Hz (^{15}N), 100 and 2000 Hz (^{1}H), and 66.7 and 933 Hz (^{13}C) at total constant-time

relaxation delays (T_{relax}) of 32 ms, 20 ms, and 30 ms for ^{15}N, ^{1}H^N, and ^{13}C' measurements, respectively. Spectra were usually acquired using sweep widths of 7.5 and 1.35 kHz as well as 512 and 120 complex points in ^{1}H and ^{15}N dimensions, respectively (at 600 MHz ^{1}H spectrometer frequency). To obtain the signs of chemical shift differences for ^{15}N, ^{1}H^N, and ^{13}C' nuclei, HSQC (^{15}N, ^{1}H^N) or HNCO (^{13}C') spectra at different static magnetic fields were recorded, as well as pairs of HSQC/HMQC spectra (^{15}N, ^{1}H^N) and pairs of HNCO spectra with single- or multiple-quantum ^{15}N-^{13}CO coherence evolution (^{13}C') at the same field.[54]

Data analysis

Spectra were processed using NMRPipe[62] and analyzed in Sparky.[63] Relaxation dispersion profiles ($R_{2,eff}(\nu_{CPMG})$) were calculated from peak heights according to $R_{2,eff}(\nu_{CPMG}) = -1/T_{relax} \ln(I(\nu_{CPMG})/I_0)$ with $I(\nu_{CPMG})$ the peak height in the spectrum recorded with CPMG frequency ν_{CPMG} and I_0 the peak height in a reference spectrum recorded without a CPMG pulse train. Errors $\Delta R_{2,eff}$ in $R_{2,eff}$ values were calculated as $\Delta R_{2,eff}(\nu_{CPMG}) = \sigma/(T_{relax} I(\nu_{CPMG}))$ with σ the pooled standard deviation of peak heights in duplicate measurements.[64]

Relaxation dispersion curves were first analyzed using the software CATIA,[52] http://pound.med.utoronto.ca/~flemming/catia/) performing numerical integration of the Bloch-McConnell equations for a 2-state exchange model. Dispersion profiles from individual residues and nuclei measured at two static magnetic fields were fit assuming exchange (*i.e.* using CATIA) as well as assuming no exchange (*i.e.* to a constant value of $R_{2,eff}$). Dispersion profiles were retained for further analysis if (a) assuming exchange improved the fit at the 99% confidence level according to F test statistics, (b) the difference between $R_{2,eff}$ values at minimum and maximum ν_{CPMG} values was at least 2 s^{-1} (^{15}N, ^{13}C) or 3 s^{-1} (^{1}H^N) at least at one static magnetic field, and (c) the average $\Delta R_{2,eff}$ error value of a dispersion profile was not larger than 25% at both static magnetic fields or not larger than 15% at least at one field. In the case of data recorded on labeled PX complexed with

unlabeled NT, the presence of dispersion from fast exchange already in free PX [55] constitutes an additional complication. To analyze only dispersion processes related to NT binding, only such $R_{2,eff}$ profiles were retained that exhibited dispersion not present in the absence of NT or significantly different (as judged from fitting the $R_{2,eff}$ difference profile) from that present without NT.

All available dispersion curves originating from individual peptide planes (i.e. amide ^{15}N and $^{1}H^{N}$ data for residue i and carbonyl ^{13}C' data for residue i-1) retained as described above were then fit together for each peptide plane separately to yield residue-specific values of exchange rate constant k_{ex}, minor state population p_B, chemical shift differences $\Delta\omega$ between major and minor state for the respective nuclei and intrinsic transverse relaxation rate $R_{2,0}$ for each residue and nucleus at each field and each admixture. Further analysis of these dispersion profiles involved (a) fitting individual residues comprising data from all nuclei at all admixtures, assuming (residue-specific) k_{ex} and $\Delta\omega$ values to be constant across admixtures, but allowing p_B to vary, using in-house software employing the analytical Carver-Richards equation[65] (b) combined fitting of data from all nuclei and all residues at a given admixture of the two partner proteins to yield global values of k_{ex} and p_B, using numerical integration by CATIA for 2-state exchange; (c) combined fitting of all nuclei and all residues at a given admixture to a model of 3-state exchange, by way of numerical integration of the Bloch-McConnell equations using the software cpmg_fitd9 [66] kindly provided by Dmitry Korzhnev (d) combined fitting of all nuclei and all residues at all admixtures to a model of linear 3-state exchange, assuming constant values of k_{ex} and $\Delta\omega$ for the two exchange processes across different admixtures, but allowing p_B to vary with admixtures and $R_{2,0}$ to vary with each dataset, by numerical integration of the Bloch-McConnell equations using home-written software and finally (e) the program ChemEx[67] kindly provided by Guillaume Bouvignies, was used to cross check results derived from (a-d). Results were found to be entirely consistent within the different programs. The quality of fits was assessed using chi-squared

15

statistics. Note that forked 3-state models were not pursued, due to the intuitive nature of the linear models allowing for a more straightforward interpretation in terms of structural and kinetic parameters.

The parameter space for fits to dispersion data assuming 3-state exchange is vast, comprises many local minima and often exhibits correlations between parameters, such that different parameter sets can yield fits with similar chi-squared statistics. We narrowed down the space of possible solutions by first considering only the admixture of NT with 5% PX, for which the CPMG experiments yielded the best compromise between signal-to-noise and number of analyzable resonances on the one hand as well as dynamic range of $R_{2,eff}$ values on the other hand. We initially required that the total excited-state population (p_B+p_C) did not exceed the relative amount of added binding partner (i.e. 5% in this case) and that no exchange rate in the resultant model exceeded 3000 s^{-1}. Convergence was obtained by fixing the sum of p_B and p_C to 5% which, given the precision of the fit, is justified based on the measurement of K_d of the NT-PX interaction in the low micromolar range (Fig. S2). The resultant model of a 3-state linear exchange has exchange rates of $k_{ex,AB}$=(852±31)s^{-1} and $k_{ex,BC}$=(2600±493)s^{-1} as well as excited-state populations of p_B=3.7±0.1% and p_C=1.3±0.1% (at the NT admixture with 5% PX). An extended grid search with less stringent requirements on resultant k_{ex} values (cutoff at 4000s^{-1}, above the sensitivity limit of CPMG experiments) consistently yielded a value of $k_{ex,AB}$ in the range of the k_{ex} found in 2-state fits as well as ^{13}C' chemical shift changes between states A and B corresponding to those extracted from 2-state fits, as is the case for the 3-state model described above. We then tested the validity of this minimum by fixing $k_{ex,AB}$ to 850 s^{-1} and fitting populations, chemical shifts, and $k_{ex,BC}$ as free parameters. This again localized a global minimum over the resultant parametric space in the combination $k_{ex,AB}$, $k_{ex,BC}$ (850, 2650) and p_B, p_C (0.35, 0.15).

Importantly dispersion data at the other admixtures yielded very good fits using this exchange model (with $k_{ex,AB}$ and $k_{ex,BC}$ fixed) based on chi-squared statistics (Table 1) and resulted in

p_B and p_C values in the range expected from the K_d of the interaction (Fig. 5). Finally, we have analyzed data from all admixtures simultaneously using in-house software, in this case fitting $k_{ex,AB}$, $k_{ex,BC}$ globally, p_B, p_C for each admixture and the chemical shifts for each site treated globally.

To obtain $\Delta\omega$ values also for those residues of the PX binding site of NT whose dispersion curves did not meet the significance criteria described above, we ran fits (assuming 2- and 3-state exchange) to data from all residues of this region, fixing global parameters (k_{ex} and p_B for 2-state exchange, $k_{ex,AB}$, $k_{ex,BC}$, p_B, p_C for 3-state exchange) to the values obtained using only CPMG data exhibiting significant dispersion, for each admixture separately.

Signs of chemical shift differences for ^{13}C nuclei (assuming 2-state exchange) were obtained by comparing resonance positions in pairs of HNCO spectra with single- or multiple-quantum ^{15}N-^{13}CO coherence evolution (^{13}C)[54] and in spectra containing different amounts of unlabeled partner protein. The visible resonance should be closer to the excited-state resonance peak in the single-quantum spectrum and in the spectrum with a larger amount of binding partner, respectively. Chemical shift differences were considered significant if their absolute value exceeded the mean plus one standard deviation of all chemical shift differences between corresponding peaks; in addition, shift differences smaller than 1 Hz were not considered significant.

Ensemble calculations using ASTEROIDS

In order to model the conformational ensemble of NT when bound to PX, we applied the minimum ensemble approach[46] implemented in a version of the ASTEROIDS genetic algorithm for ensemble selection,[68–70] with NT ^{13}C' shifts in complex as selection criteria.[47,71] ^{13}C' shifts of PX-complexed NT were generated as the sum of free-state ^{13}C' chemical shifts and ^{13}C' $\Delta\omega$ values as obtained from the fit of the canonical model of 3-state exchange to RD data (weighted means over results from individual admixtures). A common empirical

correction of -0.25 ppm was applied to all free-state [13]C' NT chemical shifts following calibration of ASTEROIDS ensemble selection against the free-state [13]C' shifts compared to the known total helical content of the central binding site of free NT (75% in residues 479-484).[46]

We used an existing flexible-meccano[72,73] ensemble of NT conformers containing sub-ensembles for all possible helices (4 to 20 residues in length) covering residues 476 – 495 as well as a fully unfolded sub-ensemble, yielding a total of 154 sub-ensembles with 1000 conformers each.[46] Chemical shifts were calculated for all conformers using SPARTA [74] and averaged over sub-ensembles. ASTEROIDS was run to obtain the weighted combination of unfolded and helical ensembles yielding the best fit to the experimental [13]C' chemical shift data, for increasing numbers of helical conformers (n = 1, 2, 3, 4), similar to the approach using residual dipolar coupling data as described.[46] Each helical conformer thus introduced three parameters into the fit (helix start, end, and population). The data could well be fit assuming a single helix extending between residues 476 and 489, very similar to helix H2 of the free state,[46] populated to 100%. No improvement (p > 0.1) was obtained with ensembles with more helical contributions, or with a population of an unfolded conformer.

Analysis of mutational studies of NT:PX interaction

In order to perturb the observed interaction kinetics in a controlled way, two key mutations were made to NT, replacing Asp475 and Asp478 by alanines. [15]N, [1]H[N], and [13]C' RD measurements were made at concentrations of mutant NT of 190μM and PX of 6.7μM (0.035 molar ratio of PX), and compared to those measured using wild type NT at the same molar ratio of PX. Two-state global fits to all residues and nuclei of mutant NT showing dispersion yielded an exchange rate k_{ex}=(247±33)s^{-1} and a bound state population of p_B=(2.7±0.3)%. This value of p_B would correspond to a K_d of 55μM (calculated as $K_d = (1-p_B) \cdot ([P_0]/p_B - [N_0])$, with $[P_0]$ and $[N_0]$ the total concentrations of PX and NT respectively). Using this K_d

estimate to calculate the concentration of free PX ligand [P], an estimate of k_{on} can be calculated as $k_{on}=k_{ex}/([P]+K_d)$, yielding a value of $4.4 \cdot 10^6$ M^{-1}s^{-1} for the NT mutant. The same calculation using the exchange rate for the binding step of wild-type NT to PX derived from the 3-state fit to NT RD data ($k_{ex,AB}=852$s^{-1}) and the upper limit of the corresponding K_d of 60µM yields a k_{on} value of $1.4 \cdot 10^7$ M^{-1}s^{-1} using the concentrations of the NT admixture with 3.5% PX, while the experimentally determined K_d of 8µM (Fig S2) gives a k_{on} value of $4 \cdot 10^7$ M^{-1}s^{-1}.

Isothermal titration calorimetry

ITC measurements were performed on the MicroCal iTC200 (GE Healthcare, PA) at 25°C. Prior to the experiment, the proteins were dialyzed into the same ITC buffer (50 mM sodium phosphate pH 6.0, 500 mM NaCl, 2 mM β-mercaptoethanol). PX at a concentration of 750µM was titrated into a solution of NT at a concentration of 50µM. A total of 24 injections of 1.5µl were performed every 180 seconds at a stirring speed of 800 rpm. Data were analyzed using Origin (OriginLab, Northampton, MA) and yielded a dissociation constant of (8.4±0.9)µM.

ABBREVIATIONS

NT – Ntail domain of Nucleoprotein from Sendai virus. PX – C-terminal domain of Phosphoprotein from Sendai virus. NMR – Nuclear magnetic resonance. RD –Relaxation dispersion. CPMG – Carr Purcell, Meiboom, Gill.

SUPPRTING INFORMATION

Figures showing ^{1}H, ^{13}C and ^{15}N relaxation dispersion curves from NT and PX free and in complex with sub-stoichiometric mixtures of the partner protein. Figures showing results of

different data fitting procedures. This material is available free of charge via the Internet at

http://pubs.acs.org

References:

(1) Dyson, H. J.; Wright, P. E. *Nat. Rev. Mol. Cell Biol.* **2005**, *6*, 197.

(2) Dunker, A. K.; Silman, I.; Uversky, V. N.; Sussman, J. L. *Curr. Opin. Struct. Biol.* **2008**, *18*, 756.

(3) Tompa, P. *Curr. Opin. Struct. Biol.* **2011**, *21*, 419.

(4) Dunker, A. K.; Uversky, V. N. *Nat. Chem. Biol.* **2008**, *4*, 229.

(5) Davey, N. E.; Travé, G.; Gibson, T. J. *Trends Biochem. Sci.* **2011**, *36*, 159.

(6) Babu, M. M.; Kriwacki, R. W.; Pappu, R. V. *Science* **2012**, *337*, 1460.

(7) Van Roey, K.; Gibson, T. J.; Davey, N. E. *Curr. Opin. Struct. Biol.* **2012**, *22*, 378.

(8) Tompa, P.; Davey, N. E.; Gibson, T. J.; Babu, M. M. *Mol. Cell* **2014**, *55*, 161.

(9) Babu, M. M.; van der Lee, R.; de Groot, N. S.; Gsponer, J. *Curr. Opin. Struct. Biol.* **2011**, *21*, 432.

(10) Jensen, M. R.; Ruigrok, R. W.; Blackledge, M. *Curr. Opin. Struct. Biol.* **2013**.

(11) Esteban-Martín, S.; Fenwick, R. B.; Salvatella, X. *J. Am. Chem. Soc.* **2010**, *132*, 4626.

(12) Fisher, C. K.; Huang, A.; Stultz, C. M. *J. Am. Chem. Soc.* **2010**, *132*, 14919.

(13) Allison, J. R.; Varnai, P.; Dobson, C. M.; Vendruscolo, M. *J. Am. Chem. Soc.* **2009**, *131*, 18314.

(14) Forman-Kay, J. D.; Mittag, T. *Structure* **2013**, *21*, 1492.

(15) Mantsyzov, A. B.; Maltsev, A. S.; Ying, J.; Shen, Y.; Hummer, G.; Bax, A. *Protein Sci. Publ. Protein Soc.* **2014**, *23*, 1275.

(16) Sugase, K.; Dyson, H. J.; Wright, P. E. *Nature* **2007**, *447*, 1021.

(17) Mittag, T.; Marsh, J.; Grishaev, A.; Orlicky, S.; Lin, H.; Sicheri, F.; Tyers, M.; Forman-Kay, J. D. *Structure* **2010**, *18*, 494.

(18) Wang, Y.; Fisher, J. C.; Mathew, R.; Ou, L.; Otieno, S.; Sublet, J.; Xiao, L.; Chen, J.; Roussel, M. F.; Kriwacki, R. W. *Nat. Chem. Biol.* **2011**, *7*, 214.

(19) Krishnan, N.; Koveal, D.; Miller, D. H.; Xue, B.; Akshinthala, S. D.; Kragelj, J.; Jensen, M. R.; Gauss, C.-M.; Page, R.; Blackledge, M.; Muthuswamy, S. K.; Peti, W.; Tonks, N. K. *Nat. Chem. Biol.* **2014**, *10*, 558.

(20) Oldfield, C. J.; Meng, J.; Yang, J. Y.; Yang, M. Q.; Uversky, V. N.; Dunker, A. K. *BMC Genomics* **2008**, *9 Suppl 1*, S1.

(21) Tompa, P.; Szász, C.; Buday, L. *Trends Biochem. Sci.* **2005**, *30*, 484.

(22) Csermely, P.; Palotai, R.; Nussinov, R. *Trends Biochem. Sci.* **2010**, *35*, 539.

(23) Kjaergaard, M.; Teilum, K.; Poulsen, F. M. *Proc. Natl. Acad. Sci. U. S. A.* **2010**, *107*, 12535.

(24) Kiefhaber, T.; Bachmann, A.; Jensen, K. S. *Curr. Opin. Struct. Biol.* **2012**, *22*, 21.

(25) Dogan, J.; Gianni, S.; Jemth, P. *Phys. Chem. Chem. Phys. PCCP* **2014**, *16*, 6323.

(26) Tompa, P.; Fuxreiter, M. *Trends Biochem. Sci.* **2008**, *33*, 2.

(27) Frauenfelder, H.; Sligar, S.; Wolynes, P. *Science* **1991**, *254*, 1598.

(28) Shoemaker, B. A.; Portman, J. J.; Wolynes, P. G. *Proc. Natl. Acad. Sci. U. S. A.* **2000**, *97*, 8868.

(29) Motlagh, H. N.; Hilser, V. J. *Proc. Natl. Acad. Sci. U. S. A.* **2012**, *109*, 4134.

(30) Liu, J.; Faeder, J. R.; Camacho, C. J. *Proc. Natl. Acad. Sci. U. S. A.* **2009**, *106*, 19819.

(31) Long, D.; Brueschweiler, R. *Plos Comput. Biol.* **2011**, *7*.

(32) Knott, M.; Best, R. B. *PLoS Comput Biol* **2012**, *8*, e1002605.

(33) Ganguly, D.; Chen, J. *J. Am. Chem. Soc.* **2009**, *131*, 5214.

(34) Zhang, W.; Ganguly, D.; Chen, J. *PLoS Comput. Biol.* **2012**, *8*, e1002353.

(35) Bachmann, A.; Wildemann, D.; Praetorius, F.; Fischer, G.; Kiefhaber, T. *Proc. Natl. Acad. Sci. U. S. A.* **2011**, *108*, 3952.

(36) Rogers, J. M.; Steward, A.; Clarke, J. *J. Am. Chem. Soc.* **2013**, *135*, 1415.

(37) Ferreon, A. C. M.; Ferreon, J. C.; Wright, P. E.; Deniz, A. A. *Nature* **2013**, *498*, 390.

(38) Wright, P. E.; Dyson, H. J. *Curr. Opin. Struct. Biol.* **2009**, *19*, 31.

(39) Palmer, A. *Chem. Rev.* **2004**, *104*, 3623.

(40) Baldwin, A. J.; Kay, L. E. *Nat. Chem. Biol.* **2009**, *5*, 808.

(41) Wishart, D. S.; Sykes, B. D. *J. Biomol. NMR* **1994**, *4*, 171.

(42) Gerard, F. C. A.; Ribeiro, E. de A., Jr; Leyrat, C.; Ivanov, I.; Blondel, D.; Longhi, S.; Ruigrok, R. W. H.; Jamin, M. *J. Mol. Biol.* **2009**, *388*, 978.

(43) Communie, G.; Ruigrok, R. W.; Jensen, M. R.; Blackledge, M. *Curr. Opin. Virol.* **2014**, *5C*, 72.

(44) Curran, J.; Homann, H.; Buchholz, C.; Rochat, S.; Neubert, W.; Kolakofsky, D. *J. Virol.* **1993**, *67*, 4358.

(45) Serrano, L.; Fersht, A. R. *Nature* **1989**, *342*, 296.

(46) Jensen, M. R.; Houben, K.; Lescop, E.; Blanchard, L.; Ruigrok, R. W. H.; Blackledge, M. *J. Am. Chem. Soc.* **2008**, *130*, 8055.

(47) Jensen, M. R.; Salmon, L.; Nodet, G.; Blackledge, M. *J. Am. Chem. Soc.* **2010**, *132*, 1270.

(48) Houben, K.; Marion, D.; Tarbouriech, N.; Ruigrok, R. W. H.; Blanchard, L. *J. Virol.* **2007**, *81*, 6807.

(49) Kingston, R. L.; Hamel, D. J.; Gay, L. S.; Dahlquist, F. W.; Matthews, B. W. *Proc. Natl. Acad. Sci. U. S. A.* **2004**, *101*, 8301.

(50) Bourhis, J.-M.; Receveur-Bréchot, V.; Oglesbee, M.; Zhang, X.; Buccellato, M.; Darbon, H.; Canard, B.; Finet, S.; Longhi, S. *Protein Sci. Publ. Protein Soc.* **2005**, *14*, 1975.

(51) McConnell, H. M. *J. Chem. Phys.* **1958**, *28*, 430.

(52) Hansen, D. F.; Vallurupalli, P.; Lundström, P.; Neudecker, P.; Kay, L. E. *J. Am. Chem. Soc.* **2008**, *130*, 2667.

(53) Wang, Y.; Jardetzky, O. *J. Am. Chem. Soc.* **2002**, *124*, 14075.

(54) Skrynnikov, N. R.; Dahlquist, F. W.; Kay, L. E. *J. Am. Chem. Soc.* **2002**, *124*, 12352.

(55) Houben, K.; Blanchard, L.; Blackledge, M.; Marion, D. *Biophys. J.* **2007**, *93*, 2830.

(56) Wang, J.; Oliveira, R. J.; Chu, X.; Whitford, P. C.; Chahine, J.; Han, W.; Wang, E.; Onuchic, J. N.; Leite, V. B. P. *Proc. Natl. Acad. Sci. U. S. A.* **2012**, *109*, 15763.

(57) Iesmantavicius, V.; Dogan, J.; Jemth, P.; Teilum, K.; Kjaergaard, M. *Angew. Chem.-Int. Ed.* **2014**, *53*, 1548.

(58) Rogers, J. M.; Wong, C. T.; Clarke, J. *J. Am. Chem. Soc.* **2014**, *136*, 5197.

(59) Hansen, D. F.; Vallurupalli, P.; Kay, L. E. *J. Phys. Chem. B* **2008**, *112*, 5898.

(60) Ishima, R.; Torchia, D. A. *J. Biomol. NMR* **2003**, *25*, 243.

(61) Lundström, P.; Hansen, D. F.; Kay, L. E. *J. Biomol. NMR* **2008**, *42*, 35.

(62) Delaglio, F.; Grzesiek, S.; Vuister, G.; Zhu, G.; Pfeifer, J.; Bax, A. *J. Biomol. NMR* **1995**, *6*, 277.

(63) Goddard, T.; Kneller, D. .

(64) Ishima, R.; Torchia, D. A. *J. Biomol. NMR* **2005**, *32*, 41.

(65) Carver, J.; Richards, R. *J. Magn. Reson.* **1972**, *6*, 89.

(66) Korzhnev, D. M.; Neudecker, P.; Mittermaier, A.; Orekhov, V. Y.; Kay, L. E. *J. Am. Chem. Soc.* **2005**, *127*, 15602.

(67) Vallurupalli, P.; Bouvignies, G.; Kay, L. E. *J. Am. Chem. Soc.* **2012**, *134*, 8148.

(68) Nodet, G.; Salmon, L.; Ozenne, V.; Meier, S.; Jensen, M. R.; Blackledge, M. *J. Am. Chem. Soc.* **2009**, *131*, 17908.

(69) Salmon, L.; Nodet, G.; Ozenne, V.; Yin, G.; Jensen, M.; Zweckstetter, M.; Blackledge, M. *J. Am. Chem. Soc.* **2010**, *132*, 8407.

(70) Ozenne, V.; Schneider, R.; Yao, M.; Huang, J.-R.; Salmon, L.; Zweckstetter, M.; Jensen, M. R.; Blackledge, M. *J. Am. Chem. Soc.* **2012**, *134*, 15138.

(71) Kragelj, J.; Ozenne, V.; Blackledge, M.; Jensen, M. R. *Chemphyschem Eur. J. Chem. Phys. Phys. Chem.* **2013**, *14*, 3034.

(72) Bernadó, P.; Blanchard, L.; Timmins, P.; Marion, D.; Ruigrok, R. W. H.; Blackledge, M. *Proc. Natl. Acad. Sci. U. S. A.* **2005**, *102*, 17002.

(73) Ozenne, V.; Bauer, F.; Salmon, L.; Huang, J.-R.; Jensen, M. R.; Segard, S.; Bernadó, P.; Charavay, C.; Blackledge, M. *Bioinforma. Oxf. Engl.* **2012**, *28*, 1463.

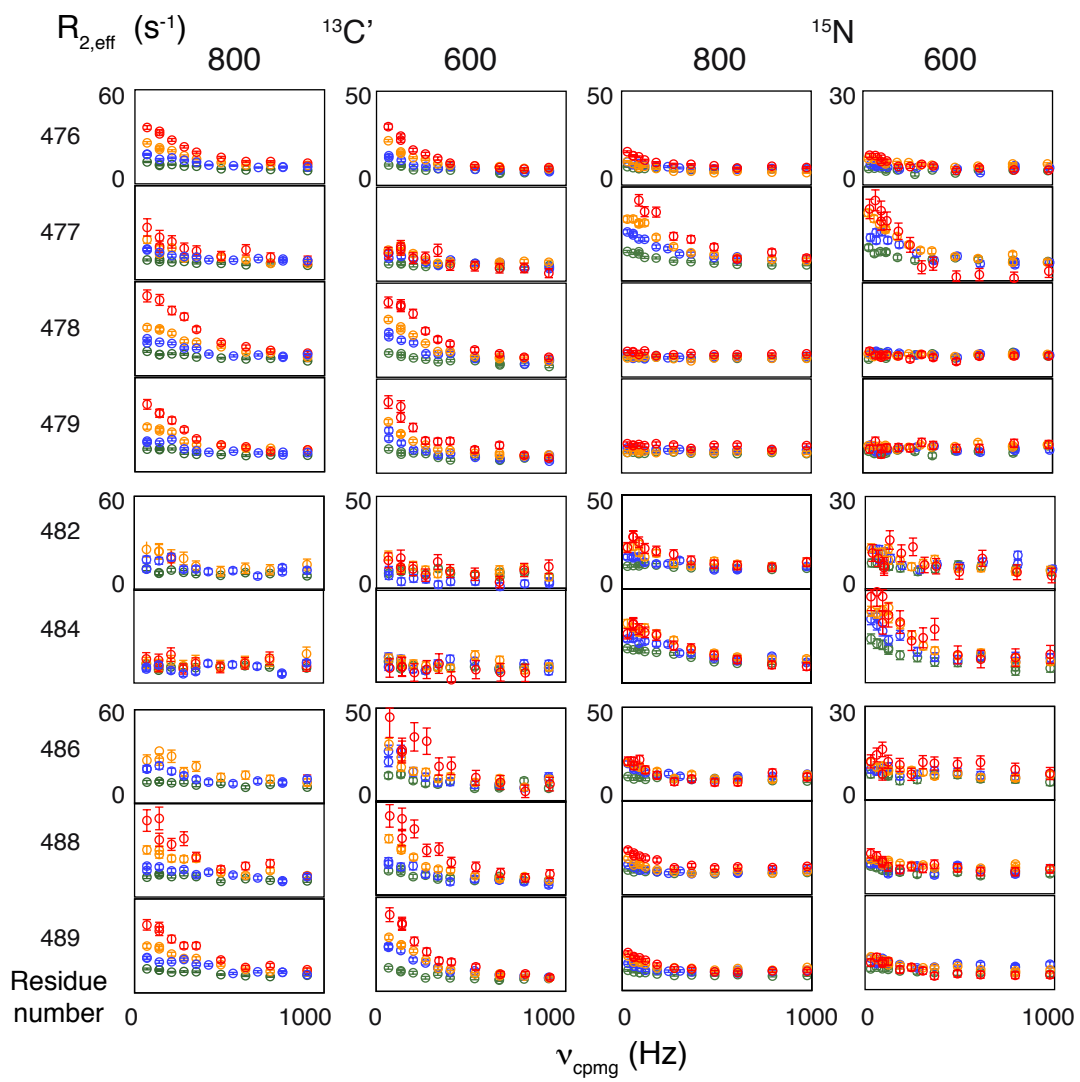(74) Shen, Y.; Bax, A. *J. Biomol. NMR* **2007**, *38*, 289.
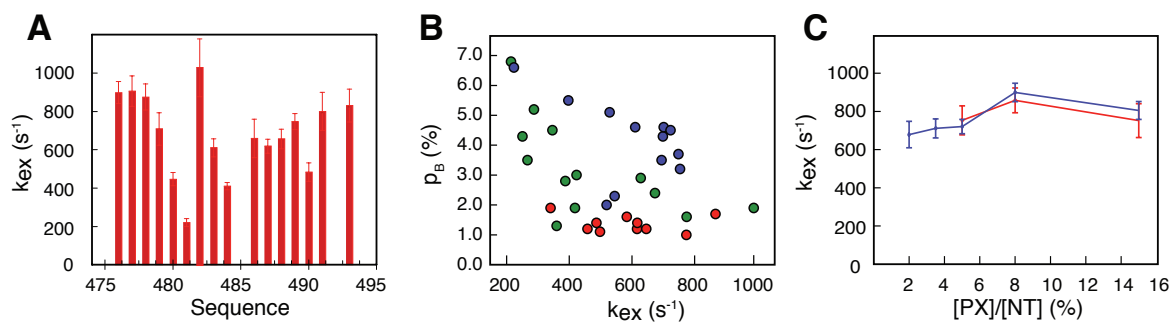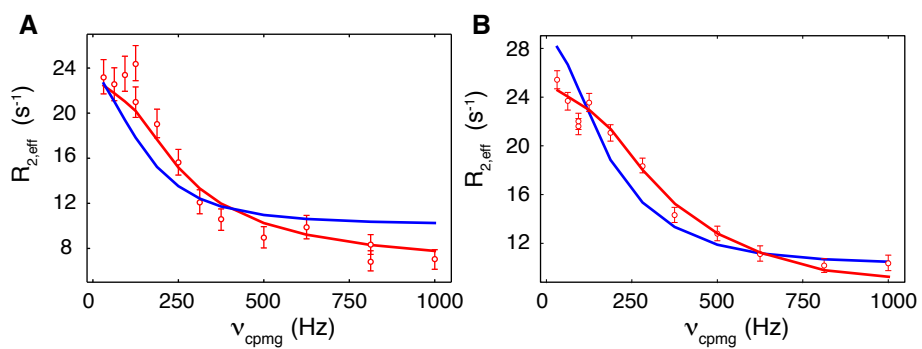
Figure 1:

Figure 2:

Figure 3:

Figure 4:
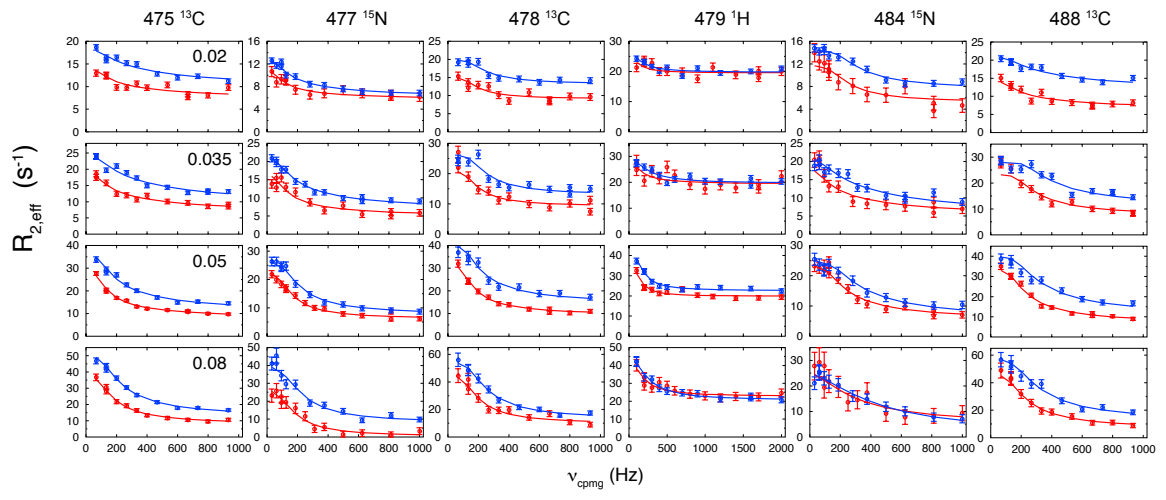
Figure 5:

Figure 6:

Figure 7:

A

B

Figure 8:

H3⁴⁷⁸⁻⁴⁹²
11%

Fast
exchange
$k_{ex} > 10^5$ s⁻¹

H2⁴⁷⁶⁻⁴⁸⁸
28%

$k_{on} > 1.5\ 10^7$ M⁻¹s⁻¹

$k_{ex} \approx 850$ s⁻¹

$k_{ex} \approx 2600$ s⁻¹

?

U
25%

H1⁴⁷⁹⁻⁴⁸⁴
36%

ΔG
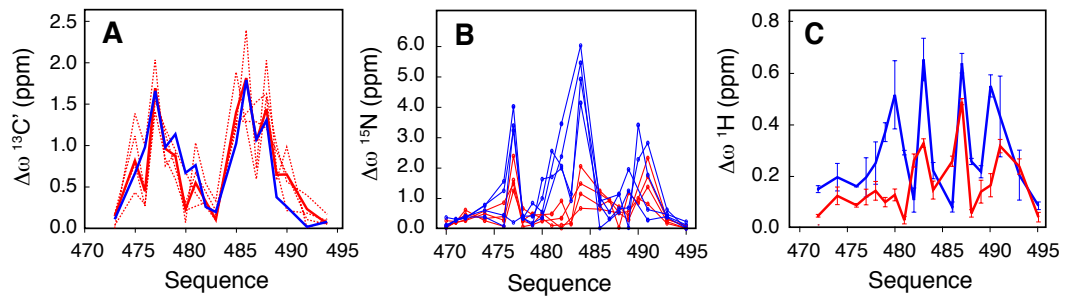
Free state
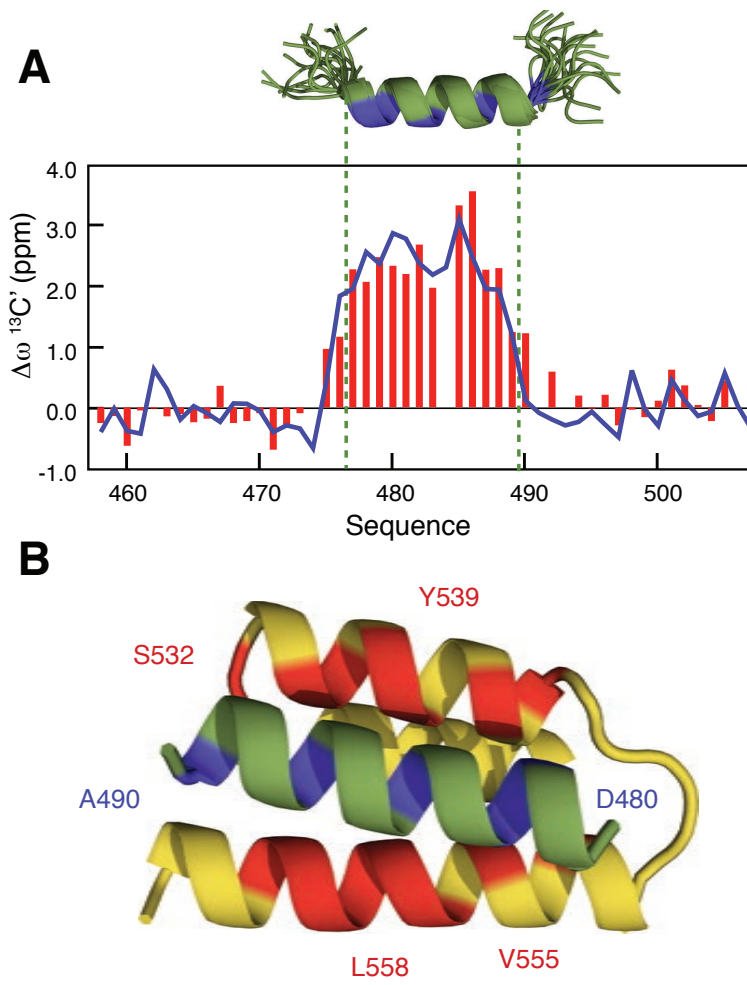equilibrium

74%

26%
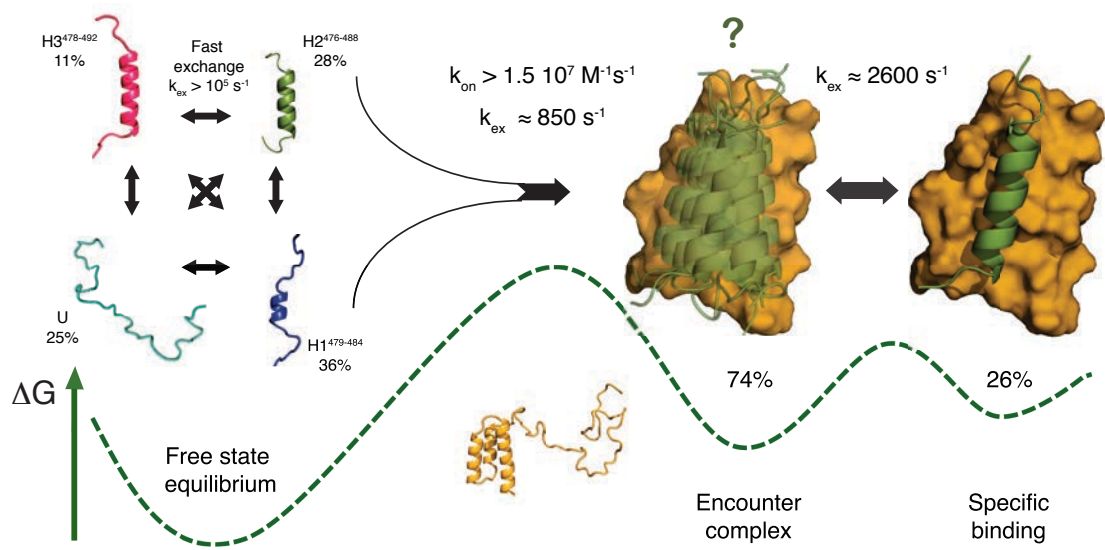
Encounter
complex

Specific
binding
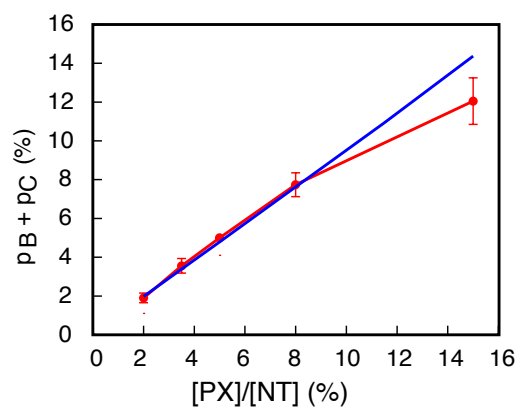
Figure Legends

Figure 1

^{13}C and ^{15}N $R_{2,eff}$ dispersion curves for selected residues measured at 14.1 and 18.8 T (600 and 800 MHz ^{1}H Larmor frequency) for 2 (green), 3.5 (blue), 5 (orange) and 8 (red) % molar ratio admixtures of PX:NT. Data from the 15% admixture and ^{1}H^N data are not shown in the interests of space. Residue number *i* refers to the peptide plane containing the amide group of residue *i* and the carbonyl carbon of residue *i*-1.

Figure 2

Kinetic parameters derived from analysis of RD data using a 2-state model.

A - Exchange rate (k_{ex}) determined from residue specific fitting of RD curves derived from all residues in the helical region from admixtures containing 2, 3.5, 5 and 8% PX using the Carver-Richards expression for two-site exchange. Data from all admixtures and all nuclei were fitted simultaneously.

B – Residue-specific exchange rates k_{ex} and excited state populations p_B for residues in the PX binding site of NT, color-coded by admixture (red - 2%, green - 3.5%, blue - 5%), obtained by fits of individual residue data to a 2-state exchange model (Fig. S5).

C – Dependence of k_{ex} values on molar ratio. Blue: k_{ex} measured for NT with respect to [PX]:[NT] molar ratio. k_{ex} values were obtained from global fits of a 2-state exchange model to NT ^{13}C', ^{15}N, and ^{1}H^N RD data at individual titration mixtures. Data can be fit using a constant $k_{ex}=(771\pm38)$s^{-1}. Red: k_{ex} measured on PX with respect to [NT]:[PX] molar ratio. k_{ex} was obtained from global fits of 2-state exchange model to ^{15}N and ^{1}H^N RD data from all sites on PX exhibiting exchange in the presence of NT, but not in the absence of NT. Data can be fit with a constant value of $k_{ex}=(803\pm37)$ s^{-1}.

Figure 3

Examples of the improvement in the reproduction of RD data from some sites when fitting all data from a single admixture assuming a single global 2-state exchange process and when

fitting all data from a single admixture assuming a single global 3-state kinetic model. Experimental ^{15}N RD data (red points) are shown for residue 484, for the 5% PX:NT admixture (blue - 2-state fit, as shown in Fig S7, red - 3-state as shown in Fig 3A.). Left hand figure shows data measured at 14.1 T, right hand figure shows data measured at 18.8 T.

Figure 4

Three-state characterization of the NT:PX interaction from RD.

Examples of fits to RD curves from NT. All data from each peptide plane in helical region were simultaneously fitted by numerical integration of the Bloch-McConnell equations for 3-state exchange with rates $k_{ex,AB}$ and $k_{ex,BC}$ (852s^{-1}, 2600s^{-1}). Solid lines - fitted curves, circles - data points (red – 14.1T, blue 18.8T).

Figure 5

Population of the PX-bound form of NT (red) determined from a simultaneous analysis of all residues showing dispersion as a function of [PX]:[NT] molar ratio. Blue line indicates the calculated p_B assuming a dissociation constant of (8.4±0.9)μM as estimated from ITC measurements (Fig. S2). Solid red line shows the fitted (p_B+p_C) values from the 3-state fit (note that for the 5% data set p_B+p_C was fixed to 5% as described in Methods).

Figure 6

Structural changes accompanying three-state exchange model for the NT:PX interaction.

A - Comparison of $\Delta\omega$(^{13}C') derived from 3-state fits. $\Delta\omega_{AB}$ from independent admixtures (molar ratios 0.02, 0.035, 0.05 and 0.08 - red dashed lines) and their weighted mean (red solid line) compared to $\Delta\omega_{AB}$ derived from analysis of all admixtures simultaneously (blue solid line).

B – Comparison of $\Delta\omega$(^{15}N) derived from the 3-state fit from molar ratio admixtures 0.02, 0.035, 0.05 and 0.08. $\Delta\omega_{AC}$ from independent admixtures (blue lines) compared to $\Delta\omega_{AB}$ from the same analysis (red lines).

C - Comparison of $\Delta\omega(^1H^N)$ derived from the 3-state fit. Weighted mean and errors (blue line) of $\Delta\omega_{AC}$ derived from analysis of all admixtures, compared to weighted means of $\Delta\omega_{AB}$ (red line).

Figure 7

Structural analysis of the different steps of NT binding to PX

A – Sum of $^{13}C'$ secondary chemical shifts of the free-state equilibrium and $\Delta\omega_{AB}$ (bars) and ASTEROIDS minimum ensemble selection against these shifts (blue). A single ensemble sub-state, reporting on helix 476-489 populated to 100% best reproduces the experimental data. The 476-489 helical sub-ensemble is shown in cartoon representation above, corresponding closely to the H2 helix (476-488), populated to 30% in the free-state ensemble. Blue residues show $\Delta\omega(^1H^N)$ values > 0.4ppm.

B – Mapping the binding site of NT with PX. Ribbon representation of NT sites showing $^1H^N$ RD derived shifts (blue) greater than the threshold ($\Delta\omega_{AC}$ $^1H^N$ > 0.4ppm). Ribbon representation of PX shows the residues (red) displaying significant ^{15}N or $^1H^N$ RD or significant shifts at all admixtures of NT. Numbers show positions of residues on PX (red) and NT (blue) residues exhibiting dispersion. The orientation of NT with respect to PX was optimized to agree with observed chemical shifts.

Figure 8

Proposed binding mechanism for Sendai virus NT to PX.

The underlying conformational equilibrium in the free state, populating three helices (H1, H2 and H3, populations of the total bound form shown in parentheses) and the unfolded form (U), binds to PX via an initial encounter complex that repopulates the equilibrium by stabilizing a helix resembling H2 with a rate of 850s^{-1}. Although the nature of the conformation of NT in the encounter complex is known, its position relative to PX is unknown in this step, although the lack of significant ^{15}N and ^1H shifts associated with this step indicate that it is highly likely that to be dynamic. This is indicated by the 'fuzzy' nature

of cartoon in the intermediate step. The association rate of this step is estimated to be faster than the diffusion limit, indicating that this encounter complex is electrostatically driven, a prediction supported by mutation studies. Following the encounter, the helix locks into the PX binding site located in the helical groove on the surface of PX at a rate (2600 s^{-1}) coincident with intrinsic motions of the PX helices. A sketch of the free-energy landscape showing that the encounter step has a higher population than the second, more specific step is shown based on populations from p=0.05 admixture.

Admixture	N data	N(param) 2-state	N(param) 3-state	χ^2 2-state	χ^2 3-state	F-test	P
2.0%	678	101	134	526.30	488.80	1.265	0.16
3.5%	726	101	134	740.50	677.51	1.668	0.01
5.0%	609	89	118	534.49	456.46	2.894	<0.0001
8.0%	556	80	106	420.54	353.60	3.276	<0.0001
15.0%	447	65	86	479.36	399.81	3.420	<0.0001

Table 1: Comparison of goodness of fit parameters for the global 2-state and global 3-state fits of data measured from NT at each different admixture of PX. In all cases except for the 2.0% admixture the 3-state fit is significantly better than the 2-state fit. The lack of significance in improvement for this admixture is probably due to signal to noise, related to the small amplitude of the RD effects at the lowest admixture.

TOC